Journal of Materials Chemistry A

Multi-funcational Ni3C Cocatalyst/g-C3N4 nanoheterojunctions for robust photocatalytic H2 evolution under Visible Light

Journal:	*Journal of Materials Chemistry A*
Manuscript ID	TA-ART-04-2018-003048.R1
Article Type:	Paper
Date Submitted by the Author:	12-May-2018
Complete List of Authors:	He, Kelin; College of Materials and Energy, South China Agricultural University Xie, Jun; South China Agricultural University, College of Materials and Energy Liu, Zhao-Qing; Guangzhou University, School of Chemistry and Chemical Engineering Li, Neng; Wuhan University of Technology, State key laboratory of silicate materials for architectures Chen, Xiaobo; University of Missouri - Kansas City, Chemistry Hu, Jun; Northwest University, Li, Xin; South China Agricultural University, College of Science;

Journal Name
Journal of Materials Chemistry A
Dynamic Article Links ►

Cite this: DOI: 10.1039/c0xx00000x

www.rsc.org/xxxxxx

ARTICLE TYPE

Multi-funcational Ni_3C Cocatalyst/g-C_3N_4 nanoheterojunctions for robust photocatalytic H_2 evolution under Visible Light

Kelin He,[a,b] Jun Xie,[a,b] Zhao-qing Liu,[c] Neng Li,[d*] Xiaobo Chen,[e] Jun Hu,[f] Xin Li, [a,b*]

Received (in XXX, XXX) Xth XXXXXXXXX 20XX, Accepted Xth XXXXXXXXX 20XX
DOI: 10.1039/b000000x

Developing highly active, non-noble-metal H_2 evolution co-catalysts is appealing yet still remains a great challenge in the promising fields of visible-light-driven photocatalytic solar fuel H_2 production. In this work, high quality hexagonal Ni_3C nanoparticles were facilely fabricated through the low-temperature thermolysis of nickel acetylacetonate in oleylamine under a nitrogen atmosphere, which were then coupled with g-C_3N_4 by the simple grinding method. The photocatalytic performances of g-C_3N_4/Ni_3C nanoheterojunctions were tested under visible light irradiation using triethanolamine (TEOA) as a hole scavenger. The optimal H_2-production rate of 15.18 μmol h^{-1} over 15 wt % Ni_3C nanoparticles decorated g-C_3N_4, corresponding to an apparent quantum yield (AQY) of 0.40% at 420 nm, is approximately 116.7 times higher than that of pure g-C_3N_4, which is even larger than that of the 0.5 wt% Pt/g-C_3N_4 sample. The well resolved density functional theory (DFT) calculation reveals that the "TOP" site of Ni_3C(113) with the H adsorption energy of -0.97 eV is likely the dominant reaction sites for H_2 evolution, rather than the Hollow and Bridge sites. It was also demonstrated by the polarization curves that the Ni_3C nanoparticles could act as multi-funcational eletcrocatalysts for improve the kinetics for water oxidation, the oxidation of TEOA, and hydrogen evolution in both acidic and basic media. Therefore, the loading of multi-funcational Ni_3C cocatalyst nanoparticles onto g-C_3N_4 can fundamentally promote the rapid transportation/separation of charge carriers, enhance oxidation kinetics of TEOA, and decrease the overpotential of H_2-evolution, thus favoring the significantly enhanced photocatalytic activity. It is highly expected that this work will provide new ideas to develop robust metal carbides as noble-metal-free cocatalysts for high-efficiency and low-cost g-C_3N_4-based photocatalytic water splitting.

1. Introduction

To address the serious environmental pollution and the increasingly intense energy crisis, hydrogen, as a renewable energy resource, has attracted wide international attention.[1, 2] Since Fujishima and Honda first demonstrated the concept of photoelectrochemical water splitting in 1972,[3] various semiconductor photocatalysts, such as oxides,[4, 5] nitrides,[6] oxynitrides,[7] sulfides,[8-12] carbides[13] and their composites, have been developed and applied in the photocatalytic hydrogen production during the past 40 years.[14] Particularly, in 2009, Wang's group first reported the photocatlytic H_2 evolution over the metal-free graphic carbon nitride (g-C_3N_4), a fascinating polymer semiconductor.[15] Since then, the g-C_3N_4 has become a shining star semiconductor and attracted tremendous attention in photocatalysis, due to its easy fabrication, high chemical and thermal stability, excellent absorption properties, low cost, environmental harmlessness, a suitable band gap and position.[16-18] However, several grand challenges, such as insufficient surface area and active sites, moderate oxidation ability, sluggish surface reaction kinetics and the rapid recombination of the electron-hole pairs, significantly lead to the low quantum efficiency of g-C_3N_4.[16, 17] Consequently, over the past eight years, a great deal of effort has been made to improve the photocatalytic performance of g-C_3N_4 by various modification approaches,[16] such as fabricating micro-/nano-structures,[19-22] improving crystalline/defect engineering,[23, 24] element doping/copolymer,[25-29] constructing heterojunctions/Z-Scheme,[30-33] coupling with nanocarbons,[34-36] dye sensitization,[37] loading cocatalysts[38-42] and their combinations[43].

Among them, one of the most effective strategies is the loading of H_2-evolution cocatalysts over g-C_3N_4, which could improve both the H_2-evolution kinetics and the separation of charges. Commonly, the noble metals, such as Pt, Ag and Au, have been extensively demonstrated to be the excellent cocatalysts for significantly improving the H_2 evolution over g-C_3N_4. However, the high cost of these noble metals, seriously restrict their commercial development and application for the g-C_3N_4-based photocatalytic H_2 evolution. Therefore, to achieve the robust photocatalytic H_2 generation, various noble metal-free H_2-

evolution electrocatalysts (e.g., Ni,[44, 45] $Ni_{12}P_5$,[46] Ni_2P,[47] CoP_x,[48, 49] Cu_3P,[50] $Ni(OH)_x$,[33, 39, 51] NiS_x,[52-54] CoS_x,[55] MoS_x,[56, 57] WS_2[58] and NiO_x[59]) have been used as cocatalysts to enhance the charge-carrier separation and the H_2-evolution kinetics on the surface of g-C_3N_4. Compared with the most widely used earth-abundant transition metals, sulfides and oxides, the nonprecious mono- and bimetallic carbides with high electronic conductivity, coverage-induced weak hydrogen adsorption and hydrophilic nature, including WC,[60-62] Ti_3C_2 MXene[63] and Mo_2C[64, 65], have been relatively seldom applied as the cocatalysts for photocatalytic H_2 evolution, despite these low-cost metal carbides[66-68] and their hybrids with nanocabons[69-71] have been employed as promising electrocatalysts for scalable electrocatalytic H_2 production. The complicated synthetic procedures of these metal carbide nanomaterials might be the possible main reasons limiting their wide applications as cocatalysts for enhancing the photocatalytic H_2 evolution over various semiconductors.

Notably, among the metal carbides, the cost effective nickel carbides have also been demonstrated experimentally to be the excellent H_2-evolution electrocatalysts.[72-74] For instance, Yang et al. reported that high-index faceted dendritic $NiC_{0.2}$ nanosheets have been found to be high performance bifunctional electrocatalysts for both the HER and OER in basic media.[74] Recently, Fan et al. fabricated Ni_3C nanocrystals encased in graphene nanoribbons,[73] and found that the resulting hybrids exhibit excellent electrocatalytic activity for the HER in acidic media and ORR in alkaline electrolytes. Similarly, it was also demonstrated that the Ni_3C nanoparticles embedded in a porous carbon network exhibited superior catalytic activity for electrocatalytic H_2 production in acidic media.[72] Clearly, the Ni_3C and Ni_3C/C hybrids could be utilized as superior electrocatalysts for the HER in both acidic and basic media, as well as for OER and ORR in alkaline electrolytes. More importantly, it was recently found that the high quality Ni_3C nanoparticles could be readily fabricated through the low-temperature thermolysis of a nickel precursor (i.e., nickel acetylacetonate) in the presence of organic surfactants (i.e., oleylamine) under inert atmosphere,[75-77] which offered a large number of new opportunities for their magnetic and catalytic applications. However, to the best of our knowledge, there is no report on exploring metallic Ni_3C as a co-catalyst for improving photocatalytic H_2-evolution activity over g-C_3N_4. Thus, these considerations have strongly motivated us to thoroughly investigate the multi-functional roles of Ni_3C cocatalysts over g-C_3N_4 in improving the photocatalytic H_2 evolution and deeply reveal their H_2-evolution mechanism.

Herein, we present the first study on the application of nickel carbide as an earth-abundant cocatalyst to significantly improve the photocatalytic H_2 evolution over g-C_3N_4. The high quality Ni_3C nanoparticles were first fabricated through the low-temperature thermolysis of nickel acetylacetonate in oleylamine under a nitrogen atmosphere. Then, the novel Ni_3C/g-C_3N_4 nanoheterojunctions were successfully synthesized by the simple grinding method. The fabrication process of the Ni_3C/g-C_3N_4 composites is shown in Scheme 1. Their photocatalytic performance was tested under visible light irradiation using TEOA as a hole scavenger. The maximum H_2-production rate of 15.18 μmol h^{-1}, corresponding to an apparent quantum yield (AQY) of 0.40% at 420 nm, is achieved by loading 15 wt% Ni_3C nanoparticles on g-C_3N_4, which is about 116.7 times higher than that of pure g-C_3N_4. The results also show that Ni_3C is better in enhancing the H_2-evolution rate than the famous noble Pt cocatalysts. The excellent catalytic activity of Ni_3C/g-C_3N_4 for both HER and OER has been investigated by the polarization curves. It is expected that this work will provide new ideas to exploit metal carbides as noble-metal-free cocatalysts for high-efficiency and low-cost g-C_3N_4-based photocatalytic water splitting.

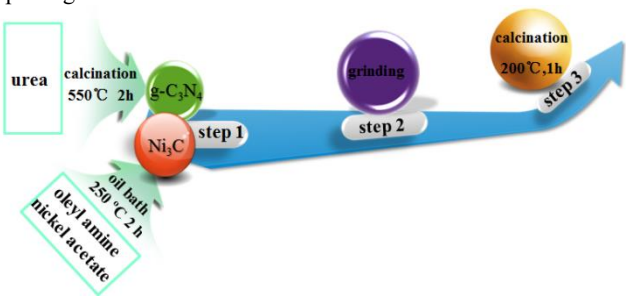

Scheme 1. Schematic illustration for the formation of Ni_3C/g-C_3N_4 photocatalysts.

2. Experimental section

2.1. Preparation of photocatalysts

2.1.1 Synthesis of g-C_3N_4 nanosheets

The pure g-C_3N_4 photocatalyst was prepared by directly heating urea without any additives. In a typical synthesis, 8 g of urea was put in a crucible with a cover，and then it was heated at 550 °C for 2 h in a muffle furnace at a heating rate of 4 °C min^{-1}.

2.1.2 Synthesis of Ni_3C nanoparticles

300 mg of nickel acetate anhydrous and 10 ml of oleylamine were put in a three-neck round-bottom flask and then stirred magnetically under a continuous flow of nitrogen. The mixture was heated and maintained at 250 ºC for 2 h. The sample is then cooled down to room temperature. 50 mL of acetone was put in three necks round bottom flask and the Ni_3C nanoparticles were precipitated by centrifugation.

2.1.3 Synthesis of Ni_3C/g-C_3N_4

In a typical synthesis procedure, g-C_3N_4 and Ni_3C nanopowder were ground together in an agate for 2 h and then the as-prepared powder was calcined at 200 °C under nitrogen flow for 1 h in a tubular furnace. The weight ratios of Ni_3C (5 wt%, 10 wt%, 15 wt% and 20 wt%) in the binary Ni_3C/g-C_3N_4 composite photocatalysts were designated as CNi5, CNi10, CNi15 and CNi20, respectively.

2.2. Characterization

The X-ray (XRD) patterns were recorded on a MSAL-XD2 diffractometer with Cu Kα radiation. X-ray photoelectron spectroscopy (XPS) data were measured with a VG ESCALAB250 surface analysis system. The transmission electron microscopy (TEM) images were recorded using a JEOL JEM-2010 electron microscope. The photoluminescence (PL) spectra were recorded using a TSC Solutions F96PRO with an excitation wavelength of 385 nm. The UV–Vis diffuse reflection

spectra (UV–Vis DRS) were performed with a VARIAN Cary-5000 UV−vis−NIR spectrophotometer. Fourier transform infrared (FTIR) spectra were recorded on a Bruker VERTEX 70 FTIR apparatus. Raman spectra were recorded at room temperature using a Renishaw InVia micro-Raman spectrometer with laser excitation at 785 nm. The Brunauer–Emmett–Teller (BET) method was used to determine the specific surface area. The pore-size distributions were derived from the desorption branches of the isotherms using the Barrett–Joyner–Halenda (BJH) method.The time-resolved decay curves of the as-fabricated samples were recorded with a FLS920 fluorescence lifetime spectrophotometer (Edinburgh Instruments, UK) under the excitation of a hydrogen flash lamp with the wavelength at 325 nm (nF900;Edinburgh Instruments).

2.3. Photocatalytic reaction procedures

Photocatalytic water splitting took place in 100 mL three-neck flask. A Xe arc lamp (350 W) with a UV cutoff filter (> 420 nm) was utilized as light source. In a typical experiment, 0.05 g of the catalyst powder was dispersed in the above reactor containing a mixed solution of 68 mL distilled water and 12 mL triethanolamine (TEOA) under ultrasound for 30 min. Before photocatalytic experiments, the above reactor was bubbled with N_2 for 30 min in order to ensure that the reaction system is under anaerobic conditions. 0.4 mL evolved gases was analyzed by a gas chromatograph (GC-7900, TCD, with Ar as carrier gas) after 1 h of illumination.

2.4 Photoelectrochemical measurement experiments

The working electrodes: 10 mg photocatalyst powder was dispersed in 4 mL ethanol containing 40 μL 0.25% Nafion solution under ultrasound for 1 h. Then, 0.5 mL of the solution dropped homogeneously on a 3 cm × 6 cm FTO glass. The as-prepared electrodes were calcined at 150 °C for 1 h (N_2 carrier gas). Transient photocurrent experiments and electrochemical impedance spectra (EIS) were measured with IM6e electrochemical workstation (Zahner Elektrik, Germany) in a standard three-electrode system using Ag/AgCl (saturated KCl) as a reference electrode，the as-prepared electrodes as the working electrodes, and a Pt plate as the counter electrode. A Xe arc lamp (350 W) with a UV-cutoff filter (λ > 420 nm) was utilized as the light source. Na_2SO_4 (0.1 mol/L) aqueous solution was utilized as the electrolyte.The bias for the photocurrent tests was 0.05 V.

2.5 Electrocatalytic hydrogen evolution.

The electrocatalytic hydrogen evolution was performed with a three-electrode cell. Linear sweep voltammetry with a 5 mV/s scan rate was performed in a 0.5 M H_2SO_4 electrolyte solution using Ag/AgCl (saturated KCl) as a reference electrode and a Pt plate as the counter electrode. The working electrodes were fabricated as follows: 6 mg of photocatalyst power was ultrasonically dispersed in 2 mL of deionized water (for >2 h)，and then 3 μL of the as-prepared solution dropped homogeneously on a glassy carbon electrode. After drying, 3 μL of 0.5% Nafion solution (contain 10 vol % ethanol) was then deposited on top of the catalyst layer.

2.6 Computational Methods

The CASTEP module of the Materials Studio software (Accelrys Inc.) was employed for the quantum chemistry calculations. During the calculations, self-consistent periodic DFT was adopted to explore the electronic structure and catalytic activities on the facets. Ionic cores were represented by an ultrasoft pseudopotential. Perdew-Burke-Ernzerhof (PBE) approximation was selected as the Generalized Gradient Approximation (GGA) method to calculate the exchange-correlation energy. The Broyden-Fletcher-Goldfarb-Shanno (BFGS) scheme was selected as the minimization algorithm. DFT-D correction was used for dispersion corrections. The energy cutoff is 380 eV and the SCF tolerance is 1.0×10-6 eV/atom. The optimization is completed when the energy, maximum force, maximum stress and maximum displacement are smaller than 5.0×10-6 eV/atom, 0.01 eV/Å, 0.02 GPa and 5.0×10-4 Å, respectively . The Gamma point only were set as k-points samplings during the calculations because there are no significant change in the calculated energies for larger k-point mesh such as 2×2×1, 3×3×1. Furthermore, at least four Ni layers were selected for reduce dispersive error. The (113) surfaces with C-terminations was built from the optimized Ni3C (space group 167, a=b=4.553 Å, c=12.920 Å) with a vacuum region of 15 Å.

3 Results and discussion

3.1 The structures and compositions of photocatalysts

X-ray diffraction (XRD) measurements were used to confirm the phase structures of the as-prepared photocatalysts. Figure 2 shows the XRD patterns of g-C_3N_4, Ni_3C, CNi5, CNi10, CNi15 and CNi20, respectively. It can be seen from Figure 1A that g-C_3N_4 exhibited two main characteristic diffraction peaks at 27.5° and 13.1°, which is correspondent with the hexagonal phase of polymeric g-C_3N_4 (JCPDS #87-1526). The strong peak of g-C_3N_4 at around 27.5° can be indexed as (002) diffraction planes of g-C_3N_4, which reflect the interlayer stacking of the aromatic system. The weak peak of g-C_3N_4 at around 13.1° can be indexed as (110) diffraction planes of g-C_3N_4, which reflect the in-planar-s-triazine structural packing motif composed of the tris-s-triazine units (ca. 0.73 nm). For the pure Ni_3C (Figure 1B), six main peaks centered at 39.5°, 41.9°, 44.9°, 58.6°, 71.2° and 78.2° can be observed, respectively, corresponding to the (110), (006), (113), (116), (300) and (119) diffraction peaks of hexagonal Ni_3C (JCPDS PDF #06-0697).[75] Notably, with increasing the loading amount of Ni_3C in the binary Ni_3C/g-C_3N_4 samples, the intensity in the diffraction (110), (006), (113) peak of Ni_3C slightly increases, while the relative diffraction peak intensity of g-C_3N_4 decreases, further confirming that the crystallinity of g-C_3N_4 in its crystal structure is markedly inhibited by the loading of Ni_3C on its surface. Figure 1C shows the Raman spectra of Ni_3C, g-C_3N_4 and CNi15. The peaks at 726 and 995 cm^{-1} are associated with the breathing modes of triazine rings. Notably, their Raman intensity of CNi15 is smaller than that of bare g-C_3N_4, which may originate from a charge transfer occurring between Ni_3C and g-C_3N_4. In addition, the peaks at 598, 1113 and 1565 cm^{-1} of CNi15 are correspondent with the Raman characteristic peaks of Ni_3C. All above results demonstrate that the Ni_3C nanoparticles are successfully loaded on the surface of g-C_3N_4, instead of the lattice doping of Ni_3C into g-C_3N_4. The FTIR spectra of CNi15

and g-C_3N_4 in the range of 500 to 3500 cm^{-1} were recorded, as shown in Figure 1D. It could be observed that the peaks at 1245, 1320, 1403 and 1452 cm^{-1} could be related to the aromatic C-N stretching, while the peaks at 1572 and 1639 cm^{-1} may be assigned to the presence of C=N bonds. In addition, the peak appeared at 808 cm^{-1} originating from condensed CN heterocycles is observed. The broad peak at 3166 cm^{-1} corresponds to the stretching vibration modes of the -NH and the adsorbed H_2O molecules. The results suggest that the intensity of g-C_3N_4 gradually decreased with the increase of Ni_3C, but the crystalline of g-C_3N_4 is unchanged.

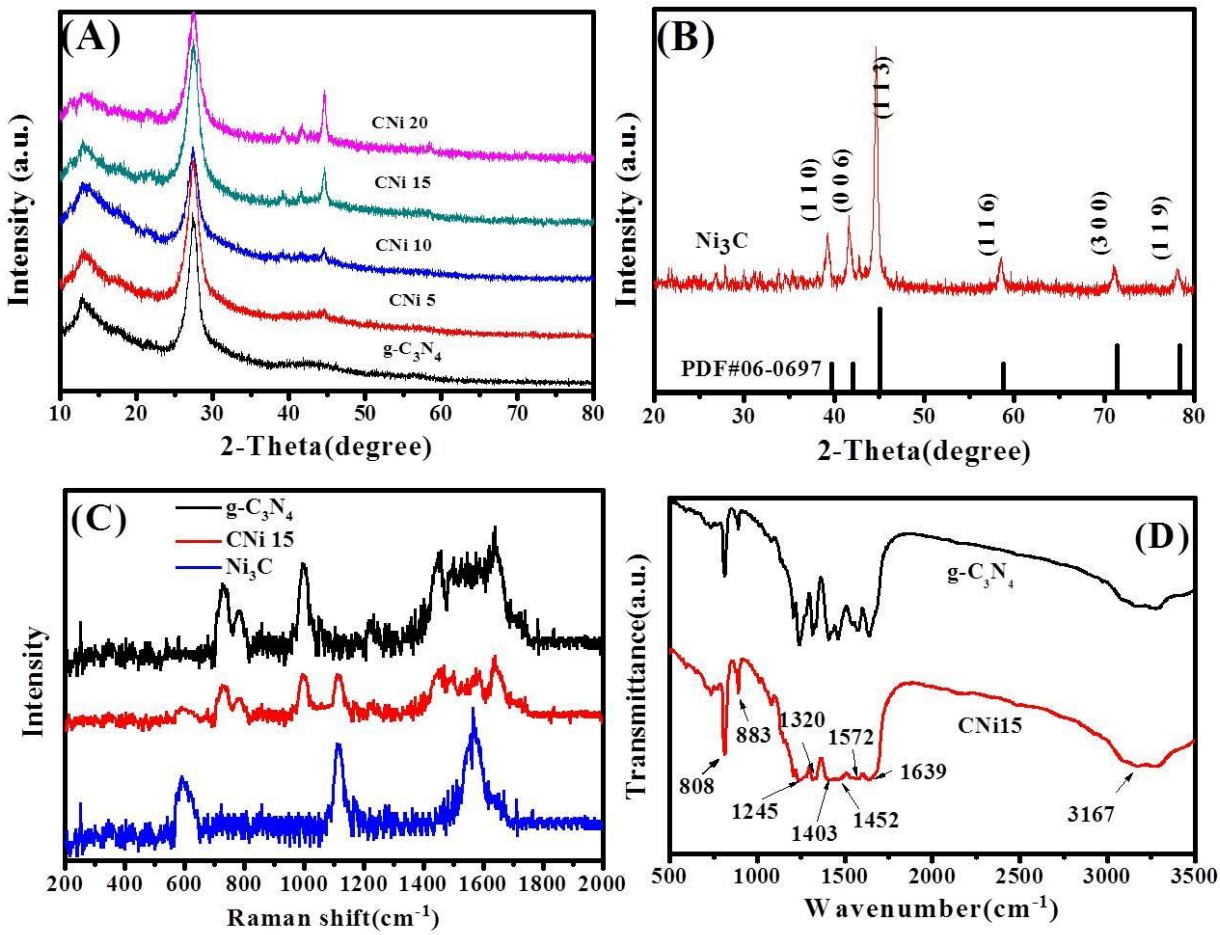

Figure 1. (A) The power XRD patterns of g-C_3N_4, CNi5, CNi10,CNi15 and CNi20, (B) The power XRD patterns of Ni_3C. (C) Raman spectra of Ni_3C, CNi15 and g-C_3N_4. (D) The FTIR spectra of CNi15 and g-C_3N_4.

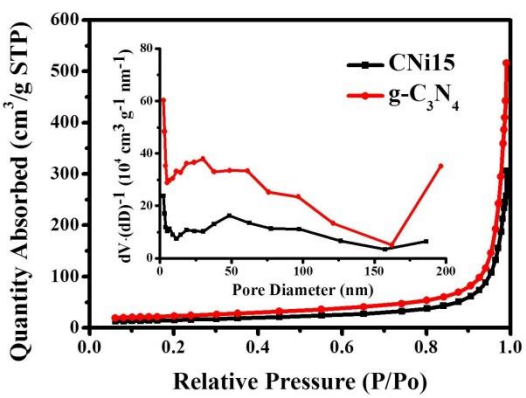

Figure 2. N_2 adsorption–desorption isotherms at 77 K and the corresponding pore size distribution curves (inset) of CNi15 and g-C_3N_4

Figure 2 displays the N_2 adsorption–desorption isotherms of the CNi15 and g-C_3N_4 samples and the corresponding pore size distributions. As shown in Figure 2, these two adsorption–desorption isotherms exhibit typical type III profiles with distinct hysteresis loops of Type H3 according to the International Union of Pure and Applied Chemistry (IUPAC) classification, indicating the predominant mesoporous character of these two photocatalysts. In addition, the pore size distributions of the CNi15 and g-C_3N_4 samples (inset in Figure 2) display a wide range of pore diameter from 3 to 180 nm, suggesting the existence of macropores and mesopores. As shown in Table 1,† the obtained BET specific surface area, average pore diameter, and pore volume of g-C_3N_4 are 80.62 m^2 g^{-1}, 34.31 nm, and 0.8007 cm^3 g^{-1}, whereas those of CNi15 are 53.85 m^2 g^{-1}, 28.21

nm, and 0.4754 cm^3 g^{-1}, respectively. It can be seen that the significantly decrease in surface area, pore size, and cumulative pore volume of CNi15 might be attributed to Ni_3C nanoparticles embedded in the pores. The results suggest that the surface area should not be the determining factor for improving the over photocatalytic H_2 evolution.

Table 1. Pore structure parameters of the CNi15 and g-C_3N_4 samples.

Samples	S_{BET}(m^2/g)	Mean pore diameter (nm)	Pore volume (cm^3 g^{-1})
g-C_3N_4	80.62	34.31	0.8007
CNi15	53.85	28.21	0.4754

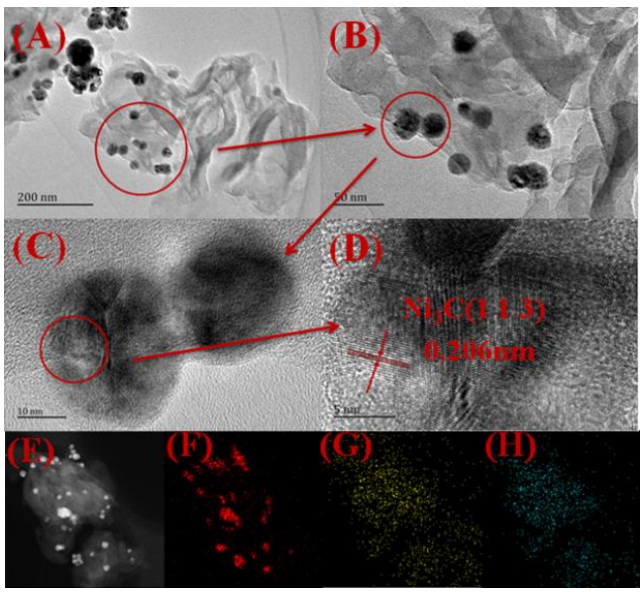

Figure 3. TEM images(A-C), HRTEM image of CNi15(D) and the corresponding EDX elemental mapping of CNi15(E-H) at the region shown in (E).

The morphology and nanostructures of CNi15 were observed by TEM and HRTEM measurements, as shown in Figure 3. The TEM images of CNi15 are displayed in Figure 3A-C, confirming that the g-C_3N_4 sample exhibits a 2D nanosheet morphology. Meanwhile, it can be clearly observed that some Ni_3C nanoparticles with diameters about 10-30 nm are uniformly distributed on the surface of g-C_3N_4, indicating the successful fabrication of g-C_3N_4/Ni_3C nanoheterojunctions. The high resolution TEM (HRTEM) images of CNi15 are shown in Figure 2D. Clearly, the obvious interplanard spacings of 0.206 nm could be observed, which is ascribed to the (113) crystallographic plane of hexagonal Ni_3C nanoparticles.[78] Moreover, the TEM and HRTEM results clearly reveal the intimate interface contacts between Ni_3C and g-C_3N_4, which is advantageous for promoting the charge transfer and increasing the active sites of catalyst, thus improving the photocatalytic activity. As shown in Figure 3E-H, the composition of surface layer is observed by the energy-dispersive X-ray spectroscopy (EDX). The EDX elemental mapping images of the CNi15 sample further demonstrate the existence of Ni, C and N elements in the CNi15 sample, which also suggest that the Ni_3C nanoparticles are uniformly loaded on the surface of g-C_3N_4. The above results confirm the successful formation of Ni_3C/g-C_3N_4 binary nanoheterojunctions.

X-ray photoelectron spectroscopy (XPS) was performed to investigate the surface chemistry and binding status of the CNi15 composites. The bonding configuration and chemical composition of the CNi15 composites are further measured by XPS. Figure 4A shows the XPS survey spectrum of the CNi15 composites, which indicates the existence of Ni, C and N in CNi15 composites, in good agreement with the above EDX elemental mapping and XRD measurement. It can be seen from Figure 4B that the symmetric peaks at 855.9 and 861.8 eV in the Ni 2p spectrum associated with Ni $2p_{3/2}$ and its satellite peak states of Ni atoms in Ni_3C, respectively, which is in keeping with the reported values of Ni_3C.[79] It can be seen from Figure 4C that two peaks at around 288.1 and 284.8eV in the C 1s spectra are ascribed to sp^2-bond carbon groups (N–C=N) in the s-triazine rings and the sp^2-bond carbon groups (C–C) of graphitic carbon, respectively.[80, 81] The peak of N 1s spectra in Figure 4D could be divided into four peaks with the binding energies of 404.6, 401.2, 399.6 and 398.6 eV.[24, 82] The main N 1s peak at 398.6 eV is ascribed to the sp^2-hybridized aromatic nitrogen groups bonded with two carbon atoms (C-N=C), demonstrating the existence of graphite-like g-C_3N_4. In addition, the peak at 399.6 eV is related to tertiary nitrogen (N–$(C)_3$). Furthermore, the peak at 401.2 eV is assigned to the sp^3-hybridized terminal amino functional groups (C–N–H). The last one at 404.6 eV originates from the π-excitation.[24] All these results fully prove that the Ni_3C nanoparticles are coupled with the surface of g-C_3N_4.

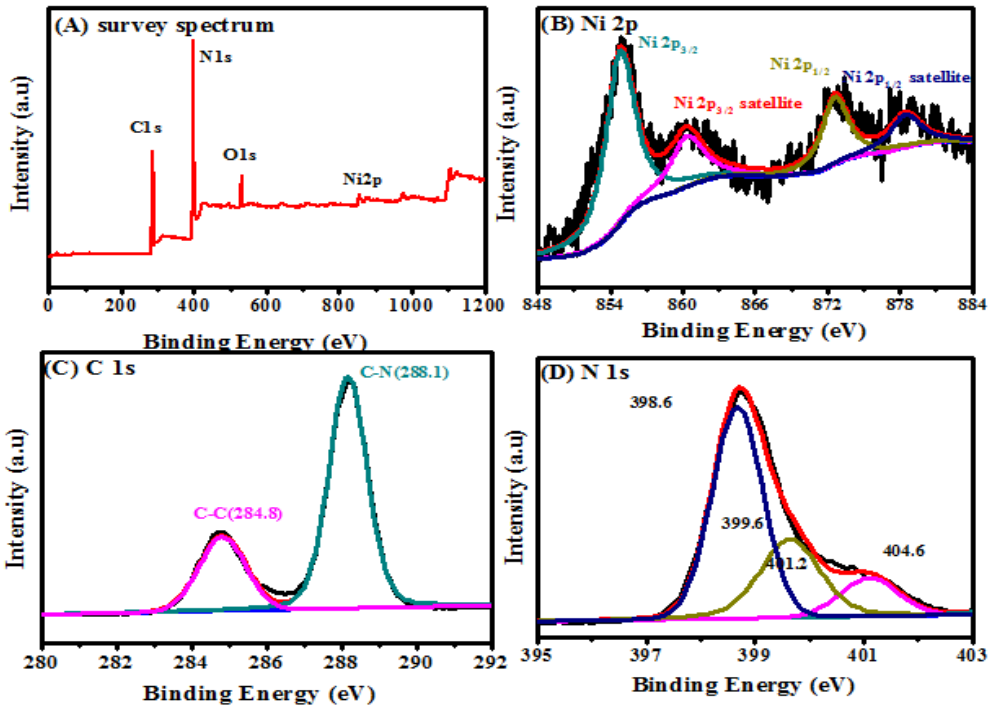

Figure 4. XPS survey spectra (A), high-resolution XPS spectra of the Ni 2p (B) C 1s (C) and N 1s (D) of the CNi15 sample.

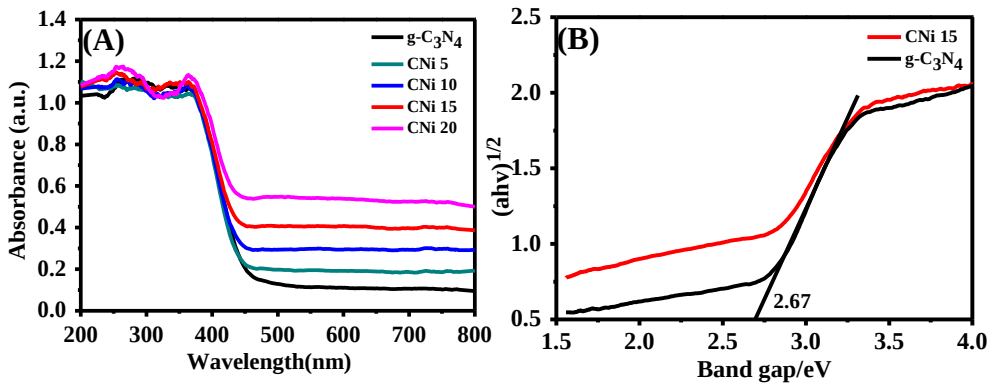

Figure 5. UV-vis absorption spectra (A) and Tauc plots of the UV-vis spectra (B) of the as-prepared photocatalysts.

3.2The optical properties of photocatalysts

The optical properties of the photocatalysts are investigated by UV-Vis diffuse reflection spectra (UV–Vis DRS). The UV−vis diffuse reflectance spectroscopy of photocatalysts is shown in Figure 5A. All composite photocatalysts show the absorption edges at around 460 nm, which is in keeping with the intrinsic band gap of g-C_3N_4. The Ni_3C nanoparticles are loaded on the surface of g-C_3N_4, with no obvious red-shift of the absorption edge of g-C_3N_4 observed, indicating that Ni_3C is not incorporated into the lattice of g-C_3N_4. In addition, the band gap (Eg) of the g-C_3N_4 semiconductor can be calculated from the following equation:

$$a = A(hv–Eg)^{n/2}/hv$$

where a, A, E_g, h and v are the absorption coefficient, proportionality constant, band energy, Planck's constant, frequency of the incident light, respectively, and n is 1 for the direct transition. Therefore, the bandgap energy of g-C_3N_4 has been calculated by the intercept of the tangents on horizontal axis in the corresponding Tauc plots of the $(ahv)^{1/2}$ versus photon energy (hv) in Figure 5B, which shows the E_g value of 2.65 eV. Notably, the introduction of Ni_3C cocatalysts has no influence on the value of E_g. However, the visible-light absorption intensity of the Ni_3C/g-C_3N_4 composites obviously increases compared with that of the pure g-C_3N_4, which is in keeping with the color changes of the composites, implying the evidently increased amount of photogenerated electron-hole pairs in the CNi15 photocatalyst, which can therefore greatly improve the photocatalytic activity of the composite samples.

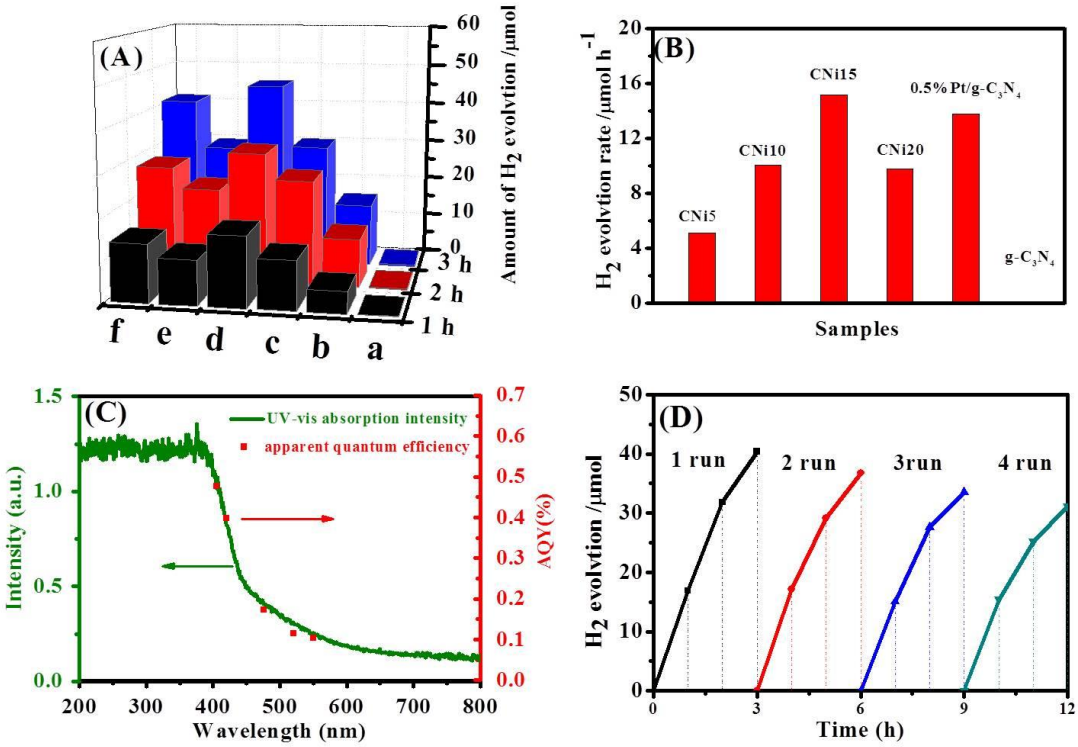

Figure 6. (A) Time courses of photocatalytic H_2 evolution: (a) g-C_3N_4, (b) CNi5, (c) CNi15, (d) CNi10, (e) CNi20 and (f)0.5 wt% Pt/g-C_3N_4. (B) The average rate of H_2-evolution of Ni_3C/g-C_3N_4 composites, g-C_3N_4 and 0.5 wt% Pt/g-C_3N_4. (C) Wavelength dependence of the apparent quantum efficiencies for the CNi15 sample. (D) Cycling tests of photocatalytic H_2-production over CNi15.

3.3 The activities and stabilities of photocatalysts

The photocatalytic H_2 production of Ni_3C/g-C_3N_4 composite photocatalyst was further measured under visible light irradiation (λ > 400nm). From Figure 6A it appears that the H_2-evolution amount of pure g-C_3N_4 is quite lower than that of g-C_3N_4 without loading the Ni_3C cocatalyst, indicating that the absence of effective active sites could led to the fast recombination of charge carriers. The total hydrogen production amounts of all photocatalysts increase linearly along with increase of time, which indicate that all of the catalysts exhibit the stable photocatalytic activity.[13] Meanwhile, the average photocatalytic H_2-production rate of CNi5, CNi10, CNi15, CNi20 and 0.5 wt% Pt/g-C_3N_4 under visible light irradiation are shown in Figure 6B. As observed in Figure 6B, the average H_2-production rates are measured to be 0.13, 5.13, 10.05, 15.18, 9.81 and 13.78 μmol h^{-1} for g-C_3N_4, CNi5, CNi10, CNi15, CNi20 and 0.5 wt% Pt/g-C_3N_4, respectively. Clearly, the highest H_2-production rate of 15.18 μmol h^{-1} is achieved by loading 15% Ni_3C nanoparticles on g-C_3N_4, which is approximately 116.7 times higher than that of pure g-C_3N_4. The excess of the Ni_3C nanoparticles can lead to the obviously decreased H_2-production rate，which can be ascribed to the inevitable mask effects. In addition, the H_2-evolution activity of CNi15 is also larger than that of 0.5 wt% Pt/g-C_3N_4 sample, further indicating that Ni_3C is a better cocatalyst than the famous noble Pt in enhancing the H_2-evolution rate over g-C_3N_4. The H_2 generation activity for CNi15 seems to be much higher than those of our previous works, such 15 wt% WC/g-C_3N_4 (7.31 μmolh^{-1})[60], 1.0 wt% $Ni(OH)_2$/g-C_3N_4 (3.6 μmol h^{-1})[51], 1.0 wt%NiS/g-C_3N_4 (9.25 μmolh^{-1})[52], wt 0.5%Ni/g-C_3N_4 (5.6 μmolh^{-1})[52] and 2.0 wt% $Ni_{12}P_5$/g-C_3N_4 (6.33 μmol h^{-1})[46], conducted under the same conditions, indicating that the Ni_3C nanoparticles are promising cocatalysts for photocatlytic H_2 evolution over g-C_3N_4.

To further investigate the activity of Ni_3C/g-C_3N_4, the wavelength-dependent apparent quantum yields (AQYs) of the CNi15 sample were measured by using various band-pass filters under different monochromatic light irradiation. The apparent quantum yields (AQYs) are displayed in Figure 6C. It can be seen that the AQY values of CNi15 are 0.48, 0.40, 0.17, 0.12 and 0.10% at 405, 420, 475, 520 and 550 nm, respectively. Additionally, the AQY decreases with an increase in the incident light wavelength, and suggests a closely coincident relationship with the UV-vis diffuse reflectance spectra (DRS) of pure g-C_3N_4. This result fully confirms that the H_2 evolution reaction is fundamentally achieved by the light absorption of g-C_3N_4, in which the Ni_3C nanoparticles only serve as a cocatalyst and electron transfer mediator to suppress the electron−hole recombination rate and boost the H_2-evolution activity.

Apart from the high H_2-evolution performance, the recycling performance and durability of a photocatalyst is another important factor influencing the practical and scalable application. To measure the stability of the CNi15 samples, the four

consecutive photocatalytic reactions over CNi15 were carried out under the same conditions. Figure 6C shows the recycling tests of CNi15 samples under visible-light irradiation for 12 hours. After four repeat reaction cycles, the activity loss (almost 23%) of the original photocatalytic H_2-production activity could be detected for the CNi15 composite, which is caused by the slow fall-off of the Ni_3C cocatalyst from g-C_3N_4, suggesting that the composite photocatalyst cannot be easily photocorroded and the relatively stable photocatalytic activity during the photocatalytic H_2-production process.

3.4. The charge-separation performances

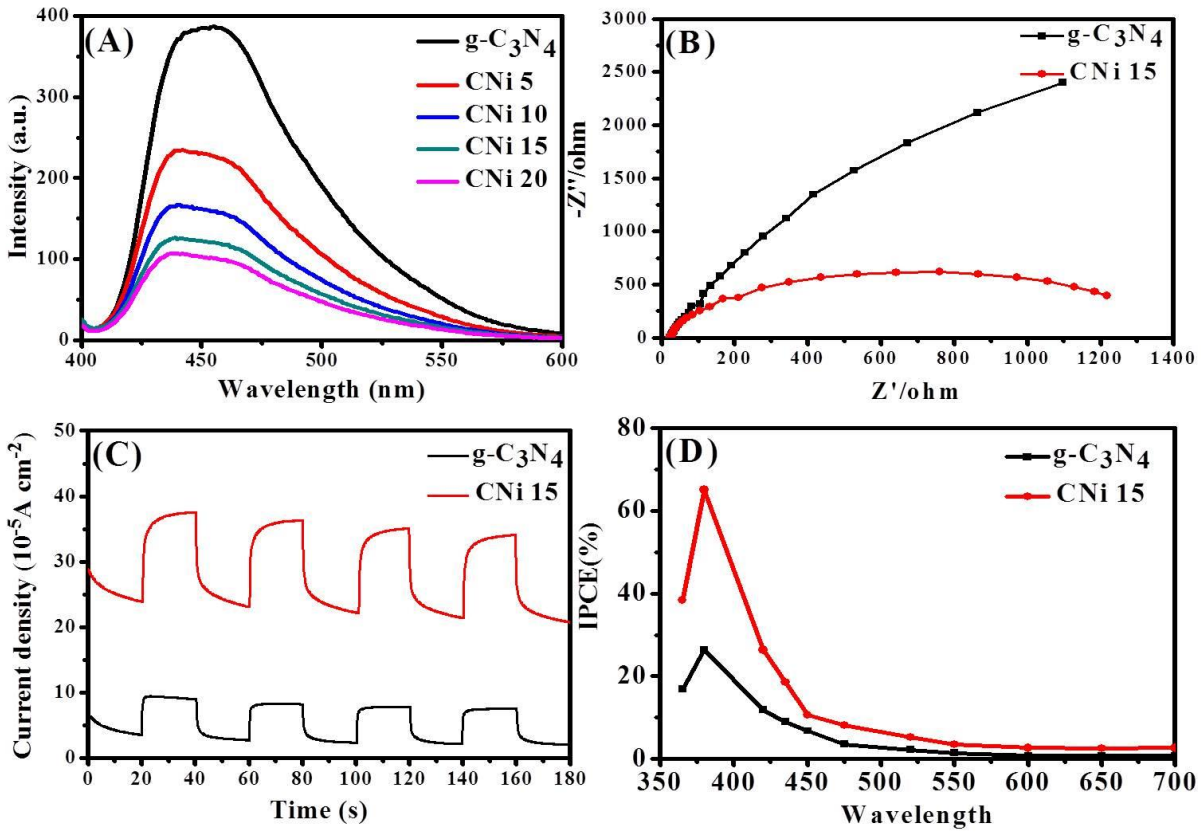

Figure 7 (A) Steady-state photoluminescence spectra of g-C_3N_4 and the composite photocatalysts. (B) Transient photocurrent responses of and CNi15 photocatalyst and g-C_3N_4. (C) Nyquist plots of CNi15 photocatalyst and g-C_3N_4. (D) The IPCE measurements of the as-prepared photocatalysts.

The charge separation of composite photocatalysts had been investigated by the room-temperature steady-state photo luminance(PL) spectra analysis. It is universally acknowledged that the PL technique is used to reveal the separation and migration processes of the photogenerated charge carriers.[24] PL spectra of g-C_3N_4, CNi5, CNi10, CNi15 and CNi20 were shown in Figure 7A. It is observed that g-C_3N_4, CNi5, CNi10, CNi15 and CNi20 show a similar broad emission peak located at around 460 nm， corresponding to the band−band PL phenomenon of g-C_3N_4 under the incident light approximately equal to its band gap energy. The intensity of the composite photocatalysts are much lower than that of pure g-C_3N_4, which is favorable for the separation of photoexcited charge carriers, further suggesting that efficient separation of photoexcited charge carriers is beneficial to increasing the photoactivities and quantum yield.

The electrochemical impedance spectra (EIS) were used to confirm the charge transfer resistance of the Ni_3C/g-C_3N_4 composites. Obviously, it is observed from Figure 7B that the arc radius in the Nyquist plot of the CNi15 photocatalyst is much smaller compared with that of g-C_3N_4, which indicates that photoexcited charge carriers are slowly recombined and effectively separated. Therefore, it is clear that Ni_3C plays important role in accelerating charge transportion and separation, which can significantly improve photocatalytic H_2-production activity. As indicated in Figure 7C, the photocurrent density of the CNi15 photocatalyst is markedly stronger under the same condition than that of pure g-C_3N_4, in accord with the PL spectra, which is caused by the fact that photogenerated electrons are transferred from the conduction band of g-C_3N_4 to Ni_3C nanoparticles. From the above results, it is demonstrated that CNi15 as cocatalysts could enhance charge mobility and suppress the recombination of photogenerated carriers, thus favoring the improved photocatalytic H_2 evolution activity.

In addition, an incident photon-to-current conversion efficiency (IPCE) of a given photocatalyst is generally employed to further

reveal the charge separation and utilization during the photocatalysis. Fig. 7D shows the comparison of IPCE spectra of CNi15 and g-C_3N_4. Notably, the IPCE value of CNi15 is much higher than that of g-C_3N_4, especially in the range of 350-550 nm. In addition, CNi15 shows a maximum efficiency of 65.8 %, while g-C_3N_4 possesses a maximum IPCE value of 26.2% at 380 nm. In addition, The IPCE values of CNi15 decrease with increasing the incident light wavelength in the range of 380-500 nm, in agreement with the wavelength-dependent AQY, clearly indicating the excellent dependence relationship between the H_2 evolution and incident light wavelength.

The separation of photo-generated charge carriers is confirmed by the fluorescence lifetime measurements, as displayed in Figure 8. The intensity-average lifetimes was calculated by the following equation: $(t) = (A_1t_1^2+ A_1t_1^2) / (A_1t_1+ A_1t_1)$. The results display that the value of g-C_3N_4 nanosheet, g-C_3N_4/0.5%Pt and CNi15 are 12.8756, 5.5446 and 3.2603 ns, respectively, which are in good agreement with the H_2-evolution activity. The above results show that the introduction of Ni_3C NPs can enhance the average fluorescence lifetime, which is beneficial for retarding the carrier recombination.

3.5 Discussion of mechanism

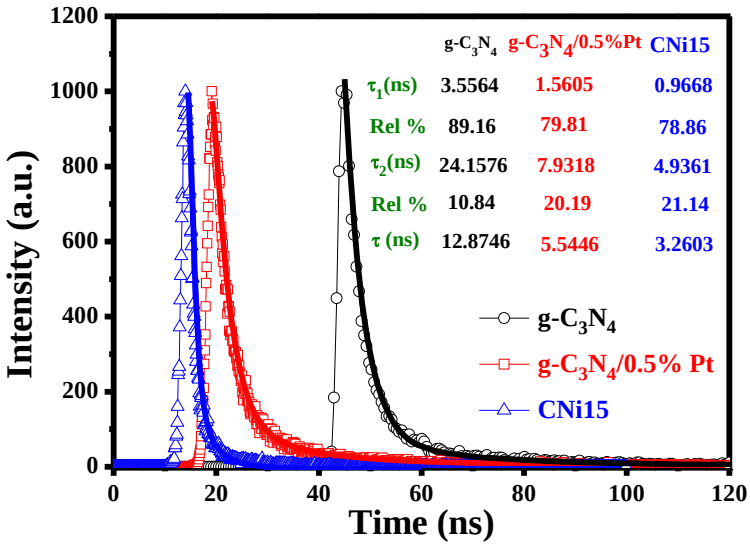

Figure 8. Time-resolved transient PL decay of CNi15, g-C_3N_4,/0.5%Pt and g-C_3N_4.

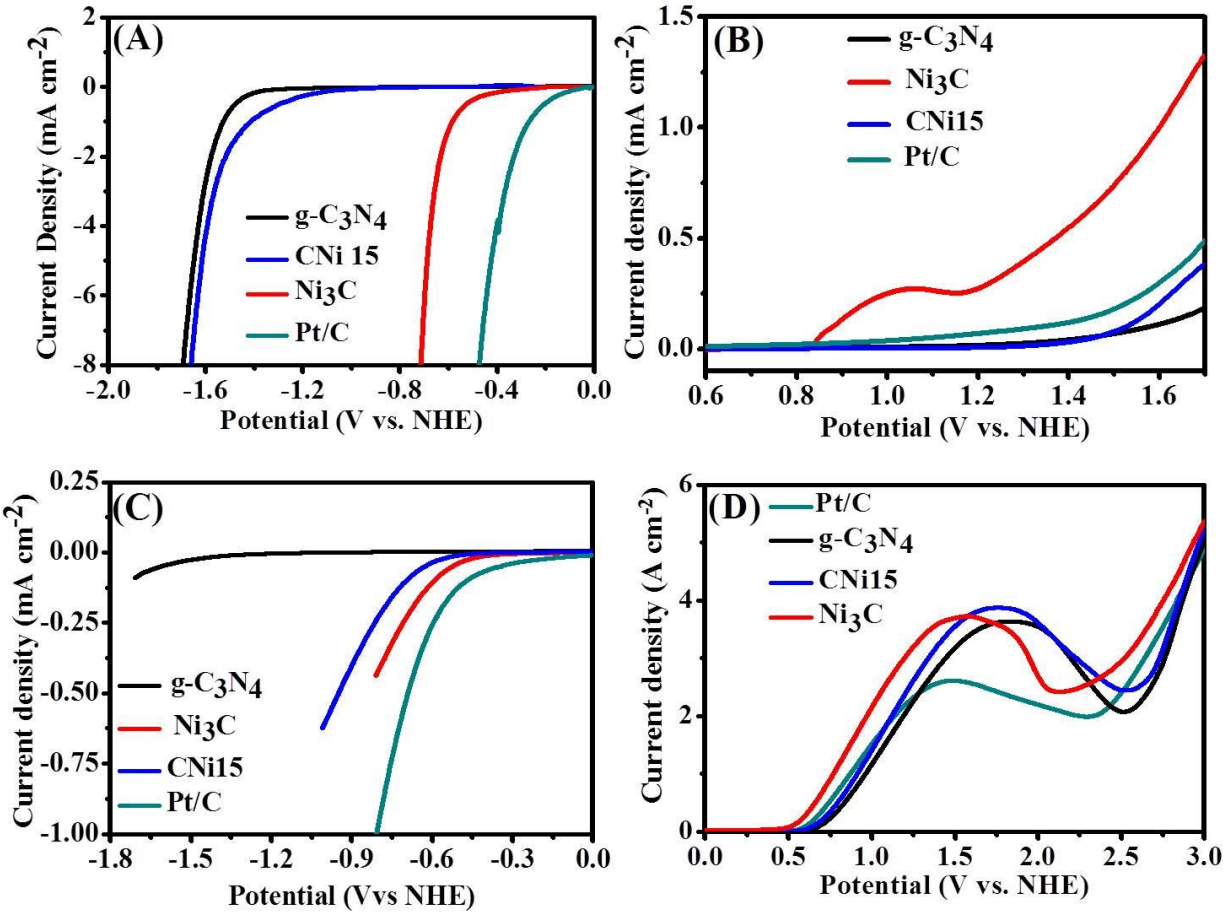

Figure 9. (A)The HER (in a 0.5 M H_2SO_4 solution) and (B) OER (in a 0.1 M NaOH solution solution) polarization curves of Ni_3C, CNi15 photocatalyst and g-C_3N_4. (C) The HER and (D) TEOA-oxidation polarization curves of Ni_3C, CNi15 photocatalyst and g-C_3N_4 in a mixed solution of 15% (v/v) TEOA and 0.1 M Na_2SO_4.

To deeply analyze the underlying photocatalytic H_2-evolution mechanism, the H_2 evolution reaction (HER) and the O_2 evolution reaction (OER) polarization curves of different samples were also performed. Figure 9A shows the HER polarization curves of Ni_3C, g-C_3N_4 and CNi15 composite photocatalysts, which could be employed to study the effects of the Ni_3C cocatalyst nnaoparticles on the H_2-evolution kinetics over g-C_3N_4. The cathodic current ranging from −0.3 to −1.8V vs Ag/AgCl is dominantly attributed to the electrocatalytic H_2 evolution. Obviously, the pure Ni_3C nanoparticles exhibit much lower electrocatalytic H_2-evolution overpotentials compared with CNi15 and g-C_3N_4, which indicates that Ni_3C as a cocatalyst plays an important role in increasing active sites and decreasing the onset potential, thereby improving the kinetics for H_2 evolution.

The OER polarization curves for CNi15, Ni_3C and C_3N_4 in 0.1 M NaOH solution are shown in Figure 9B, which provide information as to catalytic activity of water oxidation. The OER current density of CNi15, Ni_3C and C_3N_4 at 1.8 V was 0.194, 0.998 and 0.111 mA cm^{-2}, respectively. Obviously, Ni_3C photoanode presents more excellent OER activity than the other two photoanodes, thereby reducing the interface barrier of carriers such as photogenerated holes migration. Compared with the pure g-C_3N_4 photoanode, CNi15 photoanode shows a much lower anodic current density under the same conditions, indicating that Ni_3C can reduce the over potential of water oxidation. The Ni_3C/g-C_3N_4 is a potential electrocatalyst for overall water splitting.

To further prove the practical feasibility of Ni_3C/g-C_3N_4 catalysts with high efficiency for both HER and the oxidation of TEOA, the polarization curves are carried out in mixed solution of 0.1 M Na_2SO_4 and 10% (v/v) TEOA. Figure 9C shows the HER polarization curves of Ni_3C, CNi15 and g-C_3N_4. Compared with that of g-C_3N_4, the onset potential of the CNi15 is significantly lowered, proving that Ni_3C NPs could serve as the remarkable H_2-evolution active sites with the decreased onset potential. The TEOA-oxidation performance of Ni_3C, CNi15 and g-C_3N_4 are shown in Figure 9D. At a potential of 1.2 V, the TEOA-oxidation current of Ni_3C, CNi15 and g-C_3N_4 are 3.1, 2.4 and 2.0 mA cm^{-2}, respectively. It can be seen clearly that Ni_3C exhibits the lower onset potential for the oxidation of TEOA than the CNi15 and g-C_3N_4. These results further confirm the excellent catalytic activitie of Ni_3C/g-C_3N_4 for both HER and the oxidation of TEOA.

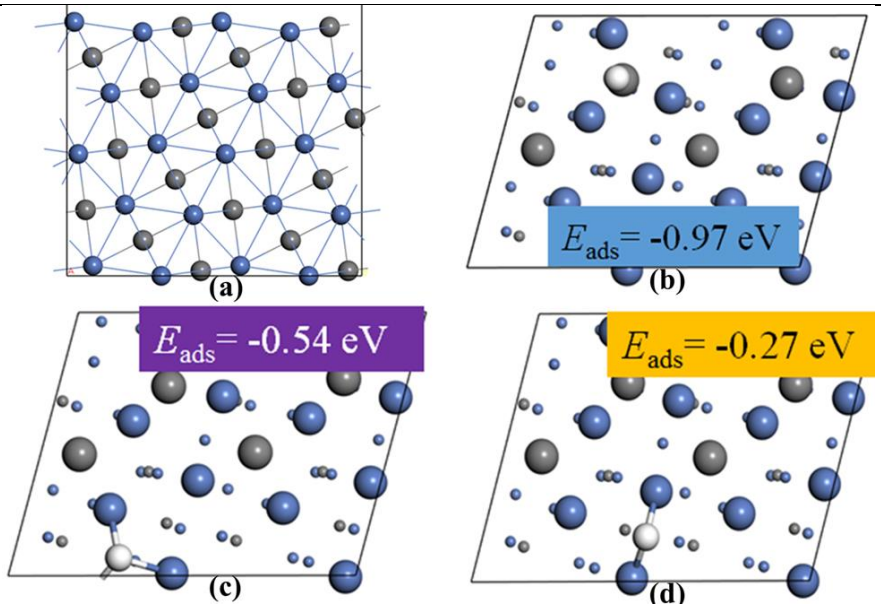

Figure 10. (a) The (113) surface model of Ni_3C, (b)-(d) H adsorption on the Ni_3C(113) surface with adsorption energy: (b) TOP; (c) Hollow; (d) Bridge (Bule: Ni; Dark: C; White: H).

To further reveal the H_2-evolution activity of Ni_3C cocatalysts, the well resolved density functional theory (DFT) calculation was performed. A schematic representation of the local structures of the (113) surface model of Ni_3C is shown in Figure 10a. Usually, the surface H adsorption energy at different locations of cocatalysts is employed as one basic factor to depict the H_2-evolution reaction activities. For the "TOP" (Figure 10b), "Hollow" (Figure 10c), and "Bridge" (Figure 10d) sites of Ni_3C(113), the H adsorption energies are -0.97, -0.54 and -0.27 eV, respectively. According to the calculated adsorption energy, one can see that the "TOP" site is more active than "Hollow" and "Bridge" sites, implying that the "TOP" site of Ni_3C(113) is likely the dominant reaction sites for H_2 evolution. Moreover, the work function of Ni_3C(113) is calculated to be about 4.85 eV, which is much higher than the work fucntion of g-C_3N_4 4.31 eV.[83] Considering to the standard hydrogen electrode energy is 4.5 eV, one can see that the photo-generated electrons could be readily injected into Ni_3C(113) and then achieve the efficient Fermi-level upshifting and finally drive the H_2 evolution reactions over Ni_3C(113) similar to electrocatalysis.[84] The calculation results further confirm the aforementioned experimental enhancement in the photocatalytic H_2 evolution over Ni_3C/g-C_3N_4 photocatalyst under visible-light irradiation.

Based on these above results, the photo-induced charge transfer mechanism of Ni_3C/g-C_3N_4 photocatalyst under visible-light irradiation is proposed, as shown in Scheme 2. It is proposed that Ni_3C nanoparticles could mainly act as cocatalysts to significantly improve the photocatalytic H_2-evolution over g-C_3N_4. Clearly, under visible-light irradiation, g-C_3N_4 is readily excited to generate the effective photo-generated electron-hole pairs due to its suitable band gap of 2.7 eV. Owing to suitable Fermi level and high electrical conductivity of Ni_3C, the photo-generated electrons are readily transferred from the conduction band of g-C_3N_4 to the Ni_3C nanoparticles, thus achieving that the photocatalytic H_2-evolution activity of g-C_3N_4 is enhanced by increasing the active sites of Ni_3C cocatalysts. The holes on the VB of g-C_3N_4 could also migrate to partial Ni_3C cocatalysts, lead to the enhanced oxidation of "TEOA" at the same time under visible light irradiation. Therefore, the loading of multi-functional Ni_3C cocatalysts onto g-C_3N_4 can promote the steady charge-carrier separation and decrease the overpotentials of H_2 evolution and TEOA oxidation, thus enhancing the photocatalytic H_2-evolution activity of g-C_3N_4. At this point, constructing the ultrafine/ultrasmall Ni_3C nanoparticles/quantum dots[85, 86] or the ultrathin Ni_3C nanosheets should be a promising strategy to further boost the their cocatalyst functions for achieving the much higher photocatalytic H_2 evolution activity, which should be paid more attention in the future studies.

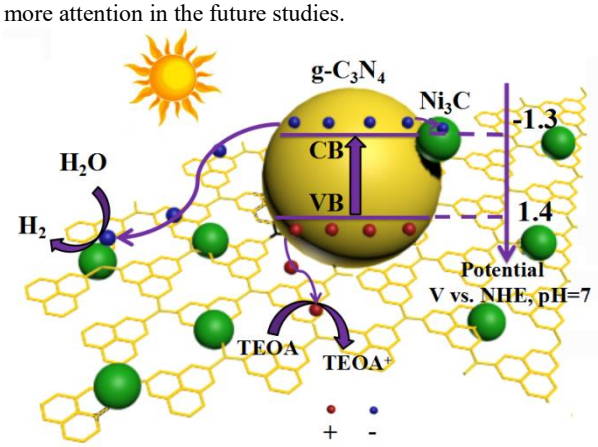

Scheme 2. Schematic illustration of the photo-induced charge separation process in the Ni_3C/g-C_3N_4 composite photocatalysts.

4 Conclusions

In summary, the novel Ni_3C/g-C_3N_4 nanoheterojunctions were successfully synthesized through simply loading the high quality hexagonal Ni_3C nanoparticles onto g-C_3N_4. The multi-function roles of Ni_3C cocatalyst nanoparticles, including the improved

electrocatalytic activity for HER, OER and oxidation of TEOA, have been thoroughly investigated by the polarization measurements. The maximum H_2-production rate of 15.18 μmol h^{-1}, corresponding to an apparent quantum yield (AQY) of 0.40% at 420 nm, is achieved by loading 15% Ni_3C nanoparticles on g-C_3N_4 under visible light irradiation using TEOA as a hole scavenger. The results demonstrated that is also larger than that of 0.5 wt% Pt/g-C_3N_4 sample. The results show that Ni_3C nanoparticles are the promising cocatalysts for photocatalytic H_2 evolution over g-C_3N_4, which are even better than the famous noble Pt cocatalysts. The well resolved density functional theory (DFT) calculation reveals that the "TOP" site of Ni_3C(113) with the H adsorption energy of -0.97 eV is likely the dominant reaction sites for H_2 evolution, rather than the Hollow and Bridge sites. Therefore, the loading of multi-functional Ni_3C cocatalysts onto g-C_3N_4 can not only promote the charge-carrier separation, but also can simultaneously act as electron- and hole- cocatalysts to improve the kinetics for H_2 generation and oxidation of TEOA and water, thus fundamentally favoring the enhanced photocatalytic activity. It is highly expected that this work will provide new ideas to fabricate noble-metal-free cocatalyst modified g-C_3N_4 photocatalysts for active and durable photocatalytic water splitting.

Acknowledgements

The work was supported by National Natural Science Foundation of China (51672089) and the State Key Laboratory of Advanced Technology for Material Synthesis and Processing (Wuhan University of Technology) (2015-KF-7) for their support.

Notes and references

[a] College of Forestry and Landscape Architecture, Key Laboratory of Energy Plants Resource and Utilization, Ministry of Agriculture, South China Agricultural University, Guangzhou 510642, PR China

[b] College of Materials and Energy, South China Agricultural University, Guangzhou 510642, PR China

[c] School of Chemistry and Chemical Engineering/ Guangzhou Key Laboratory for Environmentally Functional Materials and Technology/Key Laboratory for Water Quality and Conservation of the Pearl River Delta, Ministry of Education, Guangzhou University, Guangzhou, 510006, PR China

[d] State Key Laboratory of Silicate Materials for Architectures, Wuhan University of Technology, Wuhan 430070, PR China

[e] Department of Chemistry, University of Missouri – Kansas City, Kansas City, MO, 64110, USA.

[f] School of Chemical Engineering, Northwest University, Xi'an 710069, P. R. China

*E-mail: Xinliscau@yahoo.com (X. Li); lineng@whut.edu.cn (N. Li).

1. X. Li, J. Yu, J. Low, Y. Fang, J. Xiao and X. Chen, *J. Mater. Chem. A*, 2015, **3**, 2485-2534.
2. X. Chen, C. Li, M. Gratzel, R. Kostecki and S. S. Mao, *Chem. Soc. Rev.*, 2012, **41**, 7909–7937.
3. A. Fujishima and K. Honda, *Nature*, 1972, **238**, 37-38.
4. X. Chen and S. S. Mao, *Chem. Rev.*, 2007, **107**, 2891-2959.
5. J. Wen, X. Li, W. Liu, Y. Fang, J. Xie and Y. Xu, *Chinese Journal of Catalysis*, 2015, **36**, 2049-2070.
6. G. Hitoki, A. Ishikawa, T. Takata, J. N. Kondo, M. Hara and K. Domen, *Chem. Lett.*, 2002, **31**, 736-737.
7. G. Hitoki, T. Takata, J. N. Kondo, M. Hara, H. Kobayashi and K. Domen, *Chem. Commun.*, 2002, **38**, 1698-1699.
8. Q. Li, X. Li, S. Wageh, A. A. Al-Ghamdi and J. Yu, *Adv. Energy Mater.*, 2015, **5**, 1500010.
9. S. Ma, J. Xie, J. Wen, K. He, X. Li, W. Liu and X. Zhang, *Appl. Surf. Sci.*, 2017, **391**, 580-591.
10. J. Yuan, J. Wen, Q. Gao, S. Chen, J. Li, X. Li and Y. Fang, *Dalton Trans.*, 2015, **44**, 1680-1689.
11. S. Ma, Y. Deng, J. Xie, K. He, W. Liu, X. Chen and X. Li, *Appl. Catal. B-Environ.*, 2018, **227**, 218-228.
12. S. Ma, X. Xu, J. Xie and X. Li, *Chinese. J. Catal.*, 2017, **38**, 1970-1980.
13. X. Zhou, Q. Gao, X. Li, Y. Liu, S. Zhang, Y. Fang and J. Li, *J. Mater. Chem. A*, 2015, **3**, 10999-11005.
14. X. Chen, S. Shen, L. Guo and S. S. Mao, *Chem. Rev.*, 2010, **110**, 6503-6570.
15. X. Wang, K. Maeda, A. Thomas, K. Takanabe, G. Xin, J. Carlsson, K. Domen and M. Antonietti, *Nat. Mater.*, 2009, **8**, 76-80.
16. J. Wen, J. Xie, X. Chen and X. Li, *Appl. Surf. Sci.*, 2017, **391**, 72-123.
17. S. Cao, J. Low, J. Yu and M. Jaroniec, *Adv. Mater.*, 2015, **27**, 2150-2176.
18. S. Ye, R. Wang, M. Z. Wu and Y. P. Yuan, *Appl. Surf. Sci.*, 2015, **358**, 15-27.
19. J. Hong, S. Yin, Y. Pan, J. Han, T. Zhou and R. Xu, *Nanoscale*, 2014, **6**, 14984-14990.
20. Q. Han, B. Wang, J. Gao, Z. H. Cheng, Y. Zhao, Z. P. Zhang and L. T. Qu, *Acs Nano*, 2016, **10**, 2745-2751.
21. F. He, G. Chen, J. W. Miao, Z. X. Wang, D. M. Su, S. Liu, W. Z. Cai, L. P. Zhang, S. Hao and B. Liu, *Acs Energy Letters*, 2016, **1**, 969-975.
22. Y. X. Zeng, C. B. Liu, L. L. Wang, S. Q. Zhang, Y. B. Ding, Y. Z. Xu, Y. T. Liu and S. L. Luo, *J. Mater. Chem. A*, 2016, **4**, 19003-19010.
23. Y. Guo, J. Li, Y. Yuan, L. Li, M. Zhang, C. Zhou and Z. Lin, *Angewandte Chemie International Edition*, 2016, **55**, 14693-14697.
24. L. H. Lin, H. H. Ou, Y. F. Zhang and X. C. Wang, *Acs Catal.*, 2016, **6**, 3921-3931.
25. Y. J. Zhou, L. X. Zhang, J. J. Liu, X. Q. Fan, B. Z. Wang, M. Wang, W. C. Ren, J. Wang, M. L. Li and J. L. Shi, *J. Mater. Chem. A*, 2015, **3**, 3862-3867.
26. L. Y. Li, W. Fang, P. Zhang, J. H. Bi, Y. H. He, J. Y. Wang and W. Y. Su, *J. Mater. Chem. A*, 2016, **4**, 12402-12406.
27. J. W. Fang, H. Q. Fan, M. M. Li and C. B. Long, *J. Mater. Chem. A*, 2015, **3**, 13819-13826.
28. S. W. Cao, Q. Huang, B. C. Zhu and J. G. Yu, *J. Power. Sources.*, 2017, **351**, 151-159.
29. J. Jiang, S. Cao, C. Hu and C. Chen, *Chinese. J. Catal.*, 2017, **38**, 1981-1989.
30. J. Low, J. Yu, M. Jaroniec, S. Wageh and A. A. Al-Ghamdi, *Adv. Mater.*, 2017, **29**, 1601694.
31. F. He, G. Chen, Y. S. Zhou, Y. G. Yu, L. Q. Li, S. Hao and B. Liu, *J. Mater. Chem. A*, 2016, **4**, 3822-3827.
32. H. L. Hou, F. M. Gao, L. Wang, M. H. Shang, Z. B. Yang, J. J. Zheng and W. Y. Yang, *J. Mater. Chem. A*, 2016, **4**, 6276-6281.
33. K. He, J. Xie, X. Luo, J. Wen, S. Ma, X. Li, Y. Fang and X. Zhang, *Chinese. J. Catal.*, 2017, **38**, 240-252.
34. X. Wang, J. Cheng, H. Yu and J. Yu, *Dalton Trans.*, 2017, **46**, 6417-6424.
35. K. Li, F. Y. Su and W. D. Zhang, *Appl. Surf. Sci.*, 2016, **375**, 110-117.
36. Q. L. Xu, B. Cheng, J. G. Yu and G. Liu, *carbon*, 2017, **118**, 241-249.
37. X. H. Zhang, T. Y. Peng and S. S. Song, *J. Mater. Chem. A*, 2016, **4**, 2365-2402.
38. J. Jiang, J. Yu and S. Cao, *J. Colloid. Interf. Sci.*, 2016, **461**, 56-63.
39. J. G. Yu, S. H. Wang, B. Cheng, Z. Lin and F. Huang, *Catal. Sci. Technol.*, 2013, **3**, 1782-1789.

40. C. C. Han, Y. Lu, J. L. Zhang, L. Ge, Y. J. Li, C. F. Chen, Y. J. Xin, L. E. Wu and S. M. Fang, *J. Mater. Chem. A*, 2015, **3**, 23274-23282.
41. H. Zhao, Y. M. Dong, P. P. Jiang, H. Y. Miao, G. L. Wang and J. J. Zhang, *J. Mater. Chem. A*, 2015, **3**, 7375-7381.
42. F. Chen, H. Yang, W. Luo, P. Wang and H. Yu, *Chinese. J. Catal.*, 2017, **38**, 1990-1998.
43. Y. F. Zhang, F. Mao, H. J. Yan, K. W. Liu, H. M. Cao, J. G. Wu and D. Q. Xiao, *J. Mater. Chem. A*, 2015, **3**, 109-115.
44. L. Kong, Y. Dong, P. Jiang, G. Wang, H. Zhang and N. Zhao, *J. Mater. Chem. A*, 2016, **4**, 9998-10007.
45. A. Indra, P. W. Menezes, K. Kailasam, D. Hollmann, M. Schroder, A. Thomas, A. Bruckner and M. Driess, *Chem. Commun.*, 2016, **52**, 104-107.
46. J. Wen, J. Xie, R. Shen, X. Li, X. Luo, H. Zhang, A. Zhang and G. Bi, *Dalton Trans.*, 2017, **46**, 1794-1802.
47. P. Ye, X. Liu, J. Iocozzia, Y. Yuan, L. Gu, G. Xu and Z. Lin, *J. Mater. Chem. A*, 2017, **5**, 8493-8498.
48. S.-S. Yi, J.-M. Yan, B.-R. Wulan, S.-J. Li, K.-H. Liu and Q. Jiang, *Appl. Catal. B-Environ.*, 2017, **200**, 477-483.
49. R. Shen, J. Xie, H. Zhang, A. Zhang, X. Chen and X. Li, *Acs Sustain. Chem. Eng.*, 2018, **6**, 816-826.
50. R. Shen, J. Xie, X. Lu, X. Chen and X. Li, *Acs Sustain. Chem. Eng.*, 2018, **6**, 4026-4036.
51. G. Bi, J. Wen, X. Li, W. Liu, J. Xie, Y. Fang and W. Zhang, *Rsc. Adv.*, 2016, **6**, 31497-31506.
52. J. Wen, J. Xie, H. Zhang, A. Zhang, Y. Liu, X. Chen and X. Li, *Acs Appl. Mater. Inter.*, 2017, **9**, 14031-14042.
53. J. Wen, J. Xie, Z. Yang, R. Shen, H. Li, X. Luo, X. Chen and X. Li, *Acs Sustain. Chem. Eng.*, 2017, **5**, 2224-2236.
54. K. He, J. Xie, M. Li and X. Li, *Appl. Surf. Sci.*, 2018, **430**, 208-217.
55. J. W. Fu, C. B. Bie, B. Cheng, C. J. Jiang and J. G. Yu, *Acs Sustain. Chem. Eng.*, 2018, **6**, 2767-2779.
56. H. G. Yu, P. A. Xiao, P. Wang and J. G. Yu, *Appl. Catal. B-Environ.*, 2016, **193**, 217-225.
57. Q. Gu, H. M. Sun, Z. Y. Xie, Z. W. Gao and C. Xue, *Appl. Surf. Sci.*, 2017, **396**, 1808-1815.
58. M. S. Akple, J. X. Low, S. Wageh, A. A. Al-Ghamdi, J. G. Yu and J. Zhang, *Appl. Surf. Sci.*, 2015, **358**, 196-203.
59. G. Zhang, G. Li and X. Wang, *Chemcatchem*, 2015, **7**, 2864-2870.
60. K. He, J. Xie, Z. Yang, R. Shen, Y. Fang, S. Ma, X. Chen and X. Li, *Catal. Sci. Technol.*, 2017, **7**, 1193-1202.
61. Y.-x. Pan, T. Zhou, J. Han, J. Hong, Y. Wang, W. Zhang and R. Xu, *Catal. Sci. Technol.*, 2016, **6**, 2206-2213.
62. J. S. Jang, D. J. Ham, N. Lakshminarasimhan, W. Y. Choi and J. S. Lee, *Appl. Catal. A-Gen.*, 2008, **346**, 149-154.
63. J. R. Ran, G. P. Gao, F. T. Li, T. Y. Ma, A. J. Du and S. Z. Qiao, *Nat. Commun.*, 2017, **8**.
64. B. J. Ma, H. J. Xu, K. Y. Lin, J. Li, H. J. Zhan, W. Y. Liu and C. Li, *Chemsuschem*, 2016, **9**, 820-824.
65. C. G. Morales-Guio, K. Thorwarth, B. Niesen, L. Liardet, J. Patscheider, C. Ballif and X. L. Hu, *J. Am. Chem. Soc.*, 2015, **137**, 7035-7038.
66. M. Zeng and Y. G. Li, *J. Mater. Chem. A*, 2015, **3**, 14942-14962.
67. X. M. Li, X. G. Hao, A. Abudula and G. Q. Guan, *J. Mater. Chem. A*, 2016, **4**, 11973-12000.
68. H. L. Lin, Z. P. Shi, S. N. He, X. Yu, S. N. Wang, Q. S. Gao and Y. Tang, *Chem. Sci.*, 2016, **7**, 3399-3405.
69. X. J. Yang, X. J. Feng, H. Q. Tan, H. Y. Zang, X. L. Wang, Y. H. Wang, E. B. Wang and Y. G. Li, *J. Mater. Chem. A*, 2016, **4**, 3947-3954.
70. Y. Zhou, R. G. Ma, P. X. Li, Y. F. Chen, Q. Liu, G. Z. Cao and J. C. Wang, *J. Mater. Chem. A*, 2016, **4**, 8204-8210.
71. G. Yan, C. X. Wu, H. Q. Tan, X. J. Feng, L. K. Yan, H. Y. Zang and Y. G. Li, *J. Mater. Chem. A*, 2017, **5**, 765-772.
72. H. Wang, Y. J. Cao, G. F. Zou, Q. H. Yi, J. Guo and L. J. Gao, *Acs Appl. Mater. Inter.*, 2017, **9**, 60-64.
73. X. Fan, Z. Peng, R. Ye, H. Zhou and X. Guo, *Acs Nano*, 2015, **9**, 7407-7418.
74. H. Yang, S. Luo, X. Li, S. Li, J. Jin and J. Ma, *J. Mater. Chem. A*, 2016, **4**, 18499-18508.
75. Y. Goto, K. Taniguchi, T. Omata, S. Otsuka-Yao-Matsuo, N. Ohashi, S. Ueda, H. Yoshikawa, Y. Yamashita, H. Oohashi and K. Kobayashi, *Chem. Mater.*, 2008, **20**, 4156-4160.
76. Z. L. Schaefer, K. M. Weeber, R. Misra, P. Schiffer and R. E. Schaak, *Chem. Mater.*, 2011, **23**, 2475-2480.
77. Z. Zhou, J. Wang, W. Liu, C. Yu, B. Kong, Y. Sun, H. Yang, S. Yang and W. Wang, *Nanoscale*, 2014, **6**, 12591-12600.
78. Y. Zhang, Y. Zhu, Y. Cao, D. Li, Z. Zhang, K. Wang, F. Ding, X. Wang, D. Meng, L. Fan and J. Wu, *Rsc. Adv.*, 2016, **6**, 81989-81994.
79. M. B. Zakaria, C. Li, Q. Ji, B. Jiang, S. Tominaka, Y. Ide, J. P. Hill, K. Ariga and Y. Yamauchi, *Angewandte Chemie*, 2016, **128**, 8566-8570.
80. B. Zhu, P. Xia, W. Ho and J. Yu, *Appl. Surf. Sci.*, 2015, **344**, 188-195.
81. Q. Huang, J. Yu, S. Cao, C. Cui and B. Cheng, *Appl. Surf. Sci.*, 2015, **358**, 350-355.
82. W. T. Wu, J. Q. Zhang, W. Y. Fan, Z. T. Li, L. Z. Wang, X. M. Li, Y. Wang, R. Q. Wang, J. T. Zheng, M. B. Wu and H. B. Zeng, *Acs Catal.*, 2016, **6**, 3365-3371.
83. S. Bai, X. Wang, C. Hu, M. Xie, J. Jiang and Y. Xiong, *Chem. Commun.*, 2014, **50**, 6094-6097.
84. W. Bi, L. Zhang, Z. Sun, X. Li, T. Jin, X. Wu, Q. Zhang, Y. Luo, C. Wu and Y. Xie, *Acs Catal.*, 2016, **6**, 4253-4257.
85. R. G. Ma, Y. Zhou, Y. F. Chen, P. X. Li, Q. Liu and J. C. Wang, *Angew. Chem. Int. Edit.*, 2015, **54**, 14723-14727.
86. Y. T. Xu, X. F. Xiao, Z. M. Ye, S. L. Zhao, R. G. Shen, C. T. He, J. P. Zhang, Y. D. Li and X. M. Chen, *J. Am. Chem. Soc.*, 2017, **139**, 5285-5288.